Double helical laser beams based on interfering first-order Bessel beams

Nicholas Barbieri,[1,2] Matthew Weidman,[1] Gregory Katona,[1,2] Matthieu Baudelet,[1] Zachary Roth,[3] Eric Johnson,[3] Georgios Siviloglou,[4] Demetrios Christodoulides,[4] and Martin Richardson[1,2,*]

[1]*Townes Laser Institute, CREOL—The College of Optics and Photonics, University of Central Florida, Orlando, Florida 32816, USA*
[2]*Department of Physics—The College of Sciences, University of Central Florida, Orlando, Florida 32816, USA*
[3]*Center for Optoelectronics and Optical Communications, University of North Carolina–Charlotte, Charlotte, North Carolina 28223, USA*
[4]*CREOL—The College of Optics and Photonics, University of Central Florida, Orlando, Florida 32816, USA*
**Corresponding author: mcr@creol.ucf.edu*

Received April 15, 2011; accepted May 16, 2011;
posted May 19, 2011 (Doc. ID 145974); published June 27, 2011

We demonstrate the generation of a nondiffracting double helical beam using axicons and ±1 vortex phase plates in a common-path interferometric system. Using linear diffraction theory, a simple analytical expression describing beam propagation is shown to agree with both experiments and Fresnel-diffraction-based simulations. Experiments are performed using continuous laser light in addition to ultrafast pulses, demonstrating that the common-path arrangement and the diffraction theory work equally well for both cases.

OCIS codes: 050.1940, 050.1960, 050.1970, 260.1960, 260.3160.

1. INTRODUCTION

Nondiffracting beams, a class of optical waves that are exact solutions to the Helmholtz equations and can propagate in free space without undergoing diffraction, have been a topic of interest for more than 20 years [1]. Perhaps the most extensively investigated nondiffracting beam geometry is the Bessel beam [1], a solution to the Helmholtz equation when expanded in cylindrical coordinates. Bessel–Gauss beams [2], which are aperture-limited versions of ideal Bessel beams, can be obtained in the laboratory through the use of an axicon [3,4], a circular slit and a lens in series [5], holographic plates [6,7], or a system of diffractive optical elements [8]. These techniques typically yield zeroth-order Bessel beams. Higher-order Bessel beams can be obtained using these techniques in conjunction with either azimuthal phase elements that introduce integer topological charge [9,10] or a Laguerre–Gauss beam [11,12].

More complicated beam geometries can be obtained through the superposition of multiple Bessel beams [9,13–16]. They exhibit transverse irradiance profiles that are periodic with propagation distance [17]. These beam superposition techniques have enabled the synthesis of a variety of beam structures that can be observed to rotate either as a function of propagation distance [5,17–20] or as a function of optical system parameters [21,22]. Rotating beam geometries have a wide variety of applications, including optical micromanipulation [15,16,22–24], vortex motion in Bose–Einstein condensates [25], high-resolution imaging [26–28], complex optofluidity [29], and propeller solitons [30–32].

An optical double helix can be obtained from the superposition of first-order Bessel beams, as described by Bekshaev *et al.* [33]. In this study, linear diffraction theory is used to devise a new system to generate double helical beams from Gaussian continuous beams and then demonstrated in the laboratory. Experimental extension to the pulse regime is demonstrated and shows agreement with the continuous case.

2. HELICAL BEAM GENERATION

Double helical beams were generated by superimposing J_{+1} and J_{-1} beams in a linear interferometer (Fig. 1) with a longitudinal wavenumber difference inducing a pair of rotating irradiance peaks. Each first-order Bessel beam was obtained by transmitting a Gaussian beam through an axicon to generate a J_0 beam. The axicons were preceded by vortex plates to induce a ±1 topological charge.

For this configuration, the system throughput is only limited by Fresnel reflections that occur at the surface of each optical element, beam clipping at the aperture stop, and absorption within the optical elements themselves. The main advantage of employing such a configuration over the conventional Mach–Zender layout is the simplified alignment, in particular when optimal system throughput is required. With the use of antireflective coatings and proper apertures, system power throughput of nearly 100% can be achieved with the serial configuration, with no need to modify system alignment beyond what is necessary to achieve operation.

3. THEORETICAL DESCRIPTION

Helical beam generation can be described by using the scalar diffraction theory. Starting with the Fresnel diffraction integral in cylindrical-polar coordinates,

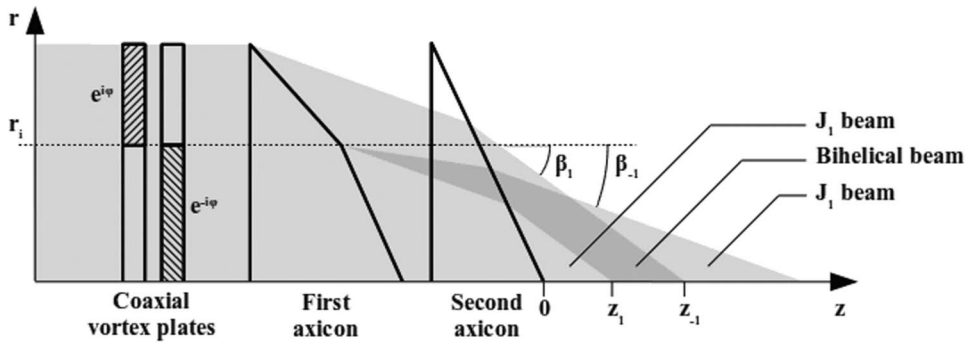

Fig. 1. Serial optical configuration for helical beam synthesis.

$$U_2(r_2,\varphi_2)=\frac{\exp(ik_0z)}{i\lambda_0 z}\exp\left[i\frac{k_0r_2^2}{2z}\right]\cdot\int_0^\infty \mathrm{d}r_1\int_0^{2\pi}\mathrm{d}\varphi_1\left[U_1(r_1,\varphi_1)r_1 \times\exp\left(i\frac{k_0r_1^2}{2z}\right)\exp\left(-i\frac{k_0r_1r_2}{z}\cos(\varphi_2-\varphi_1)\right)\right], \quad (1)$$

where U_1 is the incident scalar field, r_1,φ_1 are the polar coordinates of the incident scalar field, k_0 is the free space wavenumber, U_2 is the diffracted scalar field, r_2,φ_2 are the polar coordinates of the diffracted scalar field, and z is the propagation distance between the incident and diffracted fields.

Solving the diffraction integral requires an expression for $U_1(r_1,\varphi_1)$ obtained after transmission through a pair of coaxial vortex phase plates, and two axicons, the first of which was custom made so as to have two discrete refraction angles. This field can be obtained by evaluating the phase lag associated with the axicons and vortex plates in two radially separated regions. For the inner region, the coaxial vortex plates possess a negative unit topological charge and the first axicon possesses a 0.10° refraction angle. For the outer region, the phase plates possess a positive unit topological charge and the first axicon possesses a 0.28° refraction angle. Denote the radius separating these regions as r_i. Note that the second axicon is of conventional design and retains a constant 0.15° refraction angle throughout both regions.

Solving for the scalar field in both of these regions by taking the product of the phase lags associated with each optical element yields, for $r<r_i$,

$$\begin{aligned}U_{\text{inner}}(r,\varphi)&=\exp(-i\varphi)\times\exp(-ik_0\beta_{f_{-1}}r)\times\exp(-ik_0\beta_s)\\&=\exp(-i\varphi)\exp(-ik_0\beta_{-1}r),\end{aligned} \quad (2)$$

and for $r>r_i$,

$$\begin{aligned}U_{\text{outer}}(r,\varphi)&=\exp(i\varphi)\times\exp(-ik_0\beta_{f_1}r)\times\exp(-ik_0\beta_s r)\\&=\exp(i\varphi)\exp(-ik_0\beta_1 r),\end{aligned} \quad (3)$$

where $\exp(\pm i\varphi)$ is the vortex phase induced by the positive (outer) and negative (inner) phase plates, respectively, r_i is the radial threshold separating the topological charges on the vortex plate and the apex angles of the first axicon, $\beta_{f_1},\beta_{f_{-1}}$ are the outer and inner refraction angles associated with the first axicon, β_s is the refraction angle associated with the second axicon, and $\beta_1=\beta_{f_1}+\beta_s$ and $\beta_{-1}=\beta_{f_{-1}}+\beta_s$ are the cumulative axicon refraction angles. By combining these expressions with an incident Gaussian beam, and incorporating the effect of a thin lens of focal length f for generality, the field immediately following transmission through the optical apparatus is obtained and given by

$$\begin{aligned}U(r,\varphi)&=\sqrt{I_0}\exp\left(-\frac{r^2}{w_0^2}\right)\exp\left(-i\frac{k_0r^2}{2f}\right)[u(r-r_i)U_{\text{outer}}\\&\quad+u(r-r_i)U_{\text{inner}}]\\&=\sqrt{I_0}\exp\left(-\frac{r^2}{w_0^2}\right)\exp\left(-i\frac{k_0r^2}{2f}\right)[u(r\\&\quad-r_i)\exp(i\varphi)\exp(-ik_0\beta_1 r)\\&\quad+u(r_i-r)e^{-i\varphi}\exp(-ik_0\beta_{-1}r)],\end{aligned} \quad (4)$$

where w_0 is the Gaussian beam waist of the incident beam, $u(r)$ is the step function establishing the radial separation at $r=r_i$ between the two topological charges on the phase plates, and I_0 is the peak irradiance of the incident Gaussian beam.

The Fresnel diffraction integral can be evaluated by substituting $U(r)$ and using the Jacobi–Anger expansion:

$$\begin{aligned}\exp\left[-i\frac{k_0r_1r_2}{z}\cos(\varphi_2-\varphi_1)\right]&=\sum_{m=-\infty}^{\infty}(-i)^mJ_m\left(\frac{k_0r_1r_2}{z}\right)\\&\quad\times\exp(-im\varphi_1)\times\exp(im\varphi_2),\end{aligned} \quad (5)$$

and by observing that

$$\begin{aligned}&\frac{1}{2\pi}\int_0^{2\pi}\mathrm{d}r_1\sum_{m=-\infty}^{\infty}\exp(-im\varphi_1)\exp(im\varphi_2)[f_1(r_1,r_2)\\&\quad\times\exp(i\varphi_1)+f_{-1}(r_1,r_2)\exp(-i\varphi_1)]\\&=f_1(r_1,r_2)\exp(i\varphi_2)+f_{-1}(r_1,r_2)\exp(-i\varphi_2).\end{aligned} \quad (6)$$

This results in the new integral

$$\begin{aligned}U_2(r_2,\varphi_2)&=-\sqrt{I_0}\frac{2\pi\times\exp(ik_0z)}{\lambda_0 z}\exp\left[i\frac{k_0r_2^2}{2z}\right]\int_0^\infty\mathrm{d}r_1r_1\\&\quad\times\exp\left(-\frac{r_1^2}{w_0^2}\right)\exp\left[i\frac{k_0r_1^2}{2}\left(\frac{1}{z}-\frac{1}{f}\right)\right]G(r_1,r_2,\varphi_2),\\G&=u(r_1-r_i)J_1\left(\frac{k_0r_1r_2}{z}\right)\exp(-ik_0\beta_1r_1)\exp(i\varphi_2)\\&\quad\times-u(r_i-r_1)J_{-1}\left(\frac{k_0r_1r_2}{z}\right)\\&\quad\times\exp(-ik_0\beta_{-1}r_1)\exp(-i\varphi_2).\end{aligned} \quad (7)$$

The stationary phase approximation may be applied in Eq. (7). Evaluate the phase term that appears in both integrals:

$$\exp\left[i\left(\frac{k_0 r_1^2}{2z}\left(1-\frac{z}{f}\right)-k_0\beta_x r_1\right)\right]=\exp[i\varphi(r_1)]. \tag{8}$$

Choose r_1 such that the phase remains constant:

$$\frac{\partial\varphi}{\partial r_1}=\frac{k_0 r_1}{z}\left(1-\frac{z}{f}\right)-k_0\beta_x=0,$$
$$r_1=\beta_x z\left(1-\frac{z}{f}\right)^{-1}=F\beta_x z, \tag{9}$$

where

$$F=\left(1-\frac{z}{f}\right)^{-1} \tag{10}$$

is the compression factor, resulting from the longitudinal compression of the diffracted field caused by the thin lens moving the Fraunhofer plane from infinity to a distance f from the diffracting elements.

Evaluating at $r_1=F\beta_x z$ gives

$$U_2(r_2,\varphi_2)=-\sqrt{I_0}\frac{2\pi\,\exp(ik_0 z)}{\lambda_0}\exp\left[i\frac{k_0 r_2^2}{2z}\right][G_1(r_2,z)\exp(i_2)+G_{-1}(r_2,z)\exp(-i\varphi_2)],$$
$$G_1(r_2,z)=\beta_1 u(F\beta_1 z-r_i)\exp\left(-\frac{F^2\beta_1^2 z^2}{w_0^2}\right)\exp\left(-i\frac{F\beta_1^2 k_0 z}{2}\right)\times J_1(F\beta_1 k_0 r_2)\int_0^\infty \mathrm{d}r_1\exp\left[\frac{i}{2}\frac{\partial^2}{\partial_1^2}(r_1-F\beta_1 z)^2\right],$$
$$G_{-1}(r_2,z)=\beta_{-1}u(r_i-F\beta_{-1})\exp\left(\frac{F^2\beta_{-1}^2 z^2}{w_0^2}\right)\times\exp\left(-i\frac{F\beta_{-1}^2 k_0 z}{2}\right)J_1(F\beta_{-1}k_0 r_2)\times\int_0^\infty \mathrm{d}r_1\exp\left[\frac{i}{2}\frac{\partial^2}{\partial r_1^2}(r_1-F\beta_{-1}z)^2\right], \tag{11}$$

where

$$\int_0^\infty \mathrm{d}r\exp\left[\frac{i}{2}\frac{\partial^2}{\partial r_1^2}(r_1-F\beta_x z)^2\right]=\int_0^\infty \mathrm{d}r\exp\left[i\frac{k_0}{2Fz}(r_1-F\beta_x z)^2\right]=\frac{\sqrt{F\lambda_0 z}}{2}\exp\left(-i\frac{\pi}{4}\right). \tag{12}$$

Substituting the integral back into Eq. (11) gives

$$U(r,\varphi)=U_1(r)\exp(i\varphi)+U_{-1}(r)\exp(-i\varphi), \tag{13}$$

where

$$U_1(r)=\sqrt{I_0}e^{-i\frac{3\pi}{4}}k_1 u(z-z_1)\frac{\sqrt{F\lambda_0 z}}{2}\exp\left(-\frac{z^2}{l_{df_1}^2}\right)J_1(Fk_1 r)\times\exp\left(i\frac{k_0}{2z}r^2\right)\exp\left[i\left(k_0-\frac{Fk_1^2}{2k_0}\right)z\right],$$
$$U_{-1}(r)=\sqrt{I_0}e^{-i\frac{3\pi}{4}}k_{-1}u(z_{-1}-z)\frac{\sqrt{F\lambda_0 z}}{2}\exp\left(-\frac{z^2}{l_{df_{-1}}^2}\right)\times J_1(Fk_{-1}r)\exp\left(i\frac{k_0}{2z}r^2\right)\times\exp\left[i\left(k_0-\frac{Fk_{(-1)}^2}{2k_0}\right)z\right], \tag{14}$$

where r is the radial coordinate of the diffracted field, $k_0=\frac{2\pi}{\lambda_0}$ is the free space wavenumber, λ_0 is the wavelength of the incident beam, $k_1=\beta_1 k_0$ and $k_{-1}=\beta_{-1}k_0$ are the transverse wavenumbers, and $l_{dfx}=\frac{\omega_0}{F\beta_x}(x=1,-1)$ is the diffraction-free length for the respective fields. The limited aperture of the optical setup limits the longitudinal extent of the two superimposed Bessel beams, as dictated by

$$z_1=\frac{r_i}{F\beta_1},\qquad z_{-1}=\frac{r_i}{F\beta_{-1}}, \tag{15}$$

which, after algebraic manipulation, can be expressed as

$$z_1=\frac{r_i}{\beta_1+r_i f},\qquad z_{-1}=\frac{r_i}{\beta_{-1}+r_i f}. \tag{16}$$

For $z_1<z<z_{-1}$, which is valid only for $\beta_1>\beta_{-1}$, the two azimuthal components of the beam overlap on the optical axis. Making the substitution

$$J_1(Fk_1 r)k_1\exp\left(-\frac{z^2}{l_{df_1}^2}\right)=J_1(Fk_{-1}r)k_{-1}\exp\left(-\frac{z^2}{l_{df_{-1}}^2}\right)+\left[J_1(Fk_1 r)k_1\exp\left(-\frac{z^2}{l_{df_1}^2}\right)-J_1(Fk_{-1}r)k_{-1}\exp\left(-\frac{z^2}{l_{df_1}^2}\right)\right]$$
$$=J_1(Fk_{-1}r)k_{-1}\exp\left(-\frac{z^2}{l_{df_1}^2}\right)+B(r,z), \tag{17}$$

and observing that

$$\exp\left[i\left(k_0-\frac{Fk_1^2}{2k_0}\right)z\right]\exp(i\varphi)+\exp\left[i\left(k_0-\frac{Fk_{-1}^2}{2k_0}\right)z\right]\exp(-i\varphi)=2\cos\left(\varphi-F\frac{k_1^2-k_{-1}^2}{4k_0}\right)\exp\left[i\left(k_0-F\frac{k_1^2-k_{-1}^2}{4k_0}\right)\right], \tag{18}$$

the expression for the field within this region can be reduced to

$$U(r) = \sqrt{I_0}\exp\left(-i\frac{3\pi}{4}\right)k_{-1}\sqrt{F\lambda_0 z}\exp\left(-\frac{z^2}{l_{df_{-1}}^2}\right)J_1(Fk_{-1}r)$$
$$\times\cos\left(\varphi - F\frac{k_1^2-k_{-1}^2}{4k_0}z\right)\exp\left(i\frac{k_0}{2z}r^2\right)$$
$$\times\exp\left[i\left(k_0 - F\frac{k_1^2+k_{-1}^2}{4k_0}\right)z\right] + \sqrt{I_0}\exp\left(-i\frac{3\pi}{4}\right)$$
$$\times\frac{\sqrt{F\lambda_0 z}}{2}B(r,z)\exp(i\varphi)$$
$$\times\exp\left(i\frac{k_0}{2z}r^2\right)\exp\left[i\left(k_0 - \frac{Fk_1^2}{2k_0}\right)z\right], \quad (19)$$

which has the corresponding irradiance

$$I(r) = I_0 F\lambda_0 z k_{-1}^2\exp\left(-\frac{2z^2}{l_{df_{-1}}^2}\right)J_1^2(Fk_{-1}r)$$
$$\times\cos^2\left(\varphi - F\frac{k_1^2-k_{-1}^2}{4k_0}z\right) + \frac{I_0}{4}F\lambda_0 B^2(r,z)$$
$$+ I_0 F\lambda_0 z k_{-1}B(r,z)\exp\left(-\frac{z^2}{l_{df_{-1}}^2}\right)J_1(Fk_{-1}r)$$
$$\times\cos^2\left(\varphi - F\frac{k_1^2-k_{-1}^2}{4k_0}z\right)$$
$$= C(z)J_1^2(Fk_{-1}r)\cos^2[\theta(\varphi,z)]$$
$$+ D(r,z)J_1(Fk_{-1}r)\cos^2[\theta(\varphi,z)] + E(r,z), \quad (20)$$

where

$$\theta(\varphi,z) = \varphi - F\frac{k_1^2-k_{-1}^2}{4k_0}z. \quad (21)$$

The first term in this analytical expression for the beam irradiance describes a double helix resulting from the product of the innermost ring of the first-order Bessel function and the azimuthally dependent cosine function, which results in two distinct, isolated beam irradiance peaks. The argument of the cosine function is z dependent, and varies linearly with propagation distance, giving rise to beam rotation with propagation distance. The two irradiance peaks rotate about the optical axis at a rate given by the following relation:

$$\frac{\partial\theta}{\partial z} = \left[F\left(1+\frac{z}{f}F\right)\frac{k_1^2-k_{-1}^2}{4k_0}\right] = \frac{\pi}{2}F\left(1+\frac{z}{f}F\right)\left(\frac{\beta_1^2-\beta_{-1}^2}{\lambda_0}\right). \quad (22)$$

This beam profile is illustrated in Fig. 2.

Each irradiance peak is bounded by the first and second zero of $J_1(Fk\,r)$, placing strict upper limits on their diameter. Thus, the diameter of the irradiance peaks will not exceed

$$d_{\max} = \frac{3.8317}{Fk} = \frac{1.22}{\beta_1+\beta_{-1}}\frac{\lambda_0}{F}. \quad (23)$$

From these equations it is apparent that both the helical beam size and the rotation rate can be changed by the choice of the axicon apex angles, β_1 and β_{-1}, used in the experimental setup. This allows scaling of the helical beam rotation rate at the cost of helical beam size.

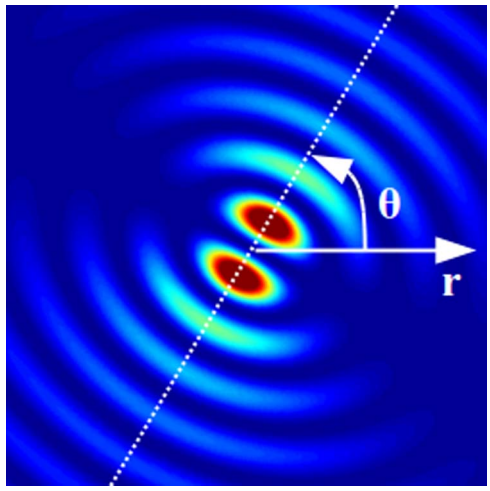

Fig. 2. (Color online) Beam profile generated from the superposition of two first-order Bessel beams.

4. NUMERICAL MODEL

A Fresnel diffraction wave solver was written in MATLAB (R2008a version 7.6.0.324) to describe two-dimensional images of the field irradiance, and to compare with experiments (Fig. 3). This numerical solver analyzed the diffraction of a scalar optical field as it propagated over a finite distance by solving the Fresnel diffraction integral. A two-dimensional fast-Fourier-transform algorithm was used to evaluate the diffraction integral. Spatially resolved phase delays were used to simulate all the optical elements in the experimental system, which were then applied to a two-dimensional representation of a Gaussian beam immediately before the MATLAB program evaluated the diffraction integral. The distance from the optical system to the output field was incorporated as a variable argument in the Fresnel diffraction integral. The initial input was a 800 nm, continuous Gaussian beam with a 12.5 mm beam waist. The optical elements used in the experimental system were modeled within the diffraction solver, which included the telescope, vortex phase plates, and both axicons.

To avoid solving the Fresnel diffraction integral several times, both the telescope and the vortex phase plates were reduced to equivalent elements. The telescope was modeled as the paraxial phase delay associated with a 2.1 m focal length thin lens, a value obtained experimentally by transmitting collimated light through the telescope and measuring the position of the resulting focal spot. The transverse scale of the vortex phase plates was rescaled based on the magnification of the phase pattern obtained using the telescope, enlarging its transverse dimensions by a factor of 5. With this modification, the vortex plate induced a unit azimuthal phase delay on incident light within a 6.25 mm diameter, and the opposite unit azimuthal phase delay outside of that diameter. The vortex plates were incorporated as unit azimuthal phase delays obtained using 16 discrete sections of constant thickness, as per the specifications of the physical element.

The thickness of both axicons were resolved in two dimensions using the three-dimensional profiler and converted to matrix format for evaluation within the diffraction solver. Using the refractive index of BK-7 glass at 800 nm, $n = 1.51$, the phase lag associated with these elements were obtained directly from the thickness matrices. The spacing between the axicons and the two equivalent elements was considered

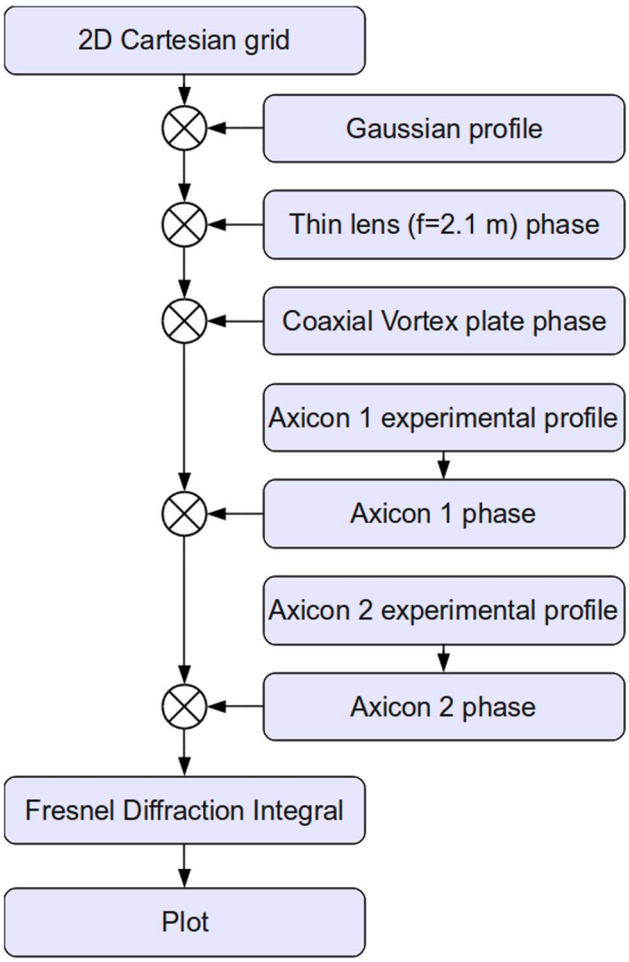

Fig. 3. (Color online) Simulation flowchart.

sufficiently small to be neglected. Thus the phase delays associated with each element were applied to the same point on the optical axis.

5. EXPERIMENTAL SETUP

The experimental setup consist of a Ti:sapphire laser, telescope, coaxial vortex plate pair, vacuum chamber, and axicon pair. Collimated light from the Ti:sapphire laser is transmitted through a telescope composed of 20 (TL1) and 60 cm (TL2) converging lenses separated by 80 cm. The vortex plate pair was placed 4 cm beyond the internal focus of telescope. Both the vortex plates and the internal focus were located within a 28 cm diameter cylindrical vacuum chamber kept at 54 mTorr to prevent plasma formation during experiments using ultrafast pulses. The axicons (A1, A2) were located 4.5 cm beyond the telescope and aligned with the optical axis.

The Ti:sapphire laser had a 290 mW output power and was used to generate both continuous and pulsed helical beams. The laser spectrum was centered at 785 nm with a FWHM spectral width of ~75 nm when mode locked that reduced to ~1 nm when operated cw. The 75 MHz pulse train from the mode-locked laser was not compensated for chirp and therefore provided pulses ~100 fs in duration as seen with intensity autocorrelation.

Fused silica vortex phase plates were fabricated using an additive microlithographic technique [34]. The vortex plates consisted of 16 azimuthal segments of constant thickness arranged to form a unit topological vortex at 800 nm. Discrete levels were first created in photoresist and then transferred to fused silica using CHF_3:O_2 inductively coupled plasma etching. The diameter of the vortex plates was limited to 5 mm; therefore, the vortex plates were positioned 4 cm behind the telescope internal focus to enable its use with beam diameters exceeding 5 mm (Fig. 4).

The vortex phase was expanded and projected onto two larger diameter axicons arranged in series (Fig. 1). The BK7 glass axicons were intentionally overfilled using a 33.5 mm beam waist Gaussian. The beam clipping on the 25 mm diameter axicons resulted in a 76% power loss. Distinct refraction angles for paraxial and marginal rays of $\beta_1 = 0.43°$ and $\beta_{-1} = 0.25°$ were created using a specially fabricated axicon with 179.7° apex angle within a 12.5 mm diameter and an equivalent apex angle of 178.6° beyond this diameter arranged in series with a 25 mm diameter axicon with 179.4° apex angle (Fig. 1). These commercially manufactured axicons were characterized using an optical surface profiler (Zygo NewView 6300).

These system parameters can be substituted into the previously derived theoretical expressions to predict the characteristics of the helical beam generated using the optical setup. Incorporating the effects of the 2.1 m beam expander focal length and using Eq. (16), the helical beam was expected to persist from $z_1 = 54$ cm to $z_{-1} = 85$ cm. From Eq. (22) and the cumulative axicon refraction angles used in the experiment, the resulting helical beam should make one complete rotation every 4.7 cm initially with the rotation accelerating until it makes a complete rotation of 3.0 cm at 85 cm. Evaluating Eq. (23) at $z = 54$ cm, maximum spot size of each irradiance peak should not exceed 54 μm.

The transverse irradiance profiles of the helical beams were evaluated using a specialized optical system. The system was comprised of two glass wedges, several neutral density filters, a single 15 mm focal length lens, and a 10× microscope objective. The system was used to attenuate and magnify the beam pattern, and to protect electronic instrumentation from damage. Incident light was reflected sequentially from both glass wedges (W1, W2), which were oriented at a 45° angle relative to the incident light, reducing power by several orders of magnitude. Attenuated light was then transmitted through the lens (L), neutral density filters (FW), and microscope objective (MO), which were arranged in series and spaced such that the optics formed an image of the first glass wedge on an ICCD camera (PI-Max 2 Model 7489 1024 × 1024 ICCD camera with a PI-ST133 controller). The imaging setup was translated along the beam to map the propagation of the double helical beam. At each position, 30 beam profiles were recorded for evaluation of the experimental fluctuations.

6. RESULTS AND DISCUSSION

Experiments were initially conducted using the 785 nm continuous laser beam. The double helical beams were observed at a distance of 60 ± 0.5 cm from the axicon pair on the optical axis, and persisted for 20 ± 0.5 cm, falling within the theoretically predicted longitudinal range.

Beam profile measurements were taken along the optical axis along the range for which the double helical beam was observed, using the imaging system. Beam transverse irradiance profiles of the helical beam were recorded along the

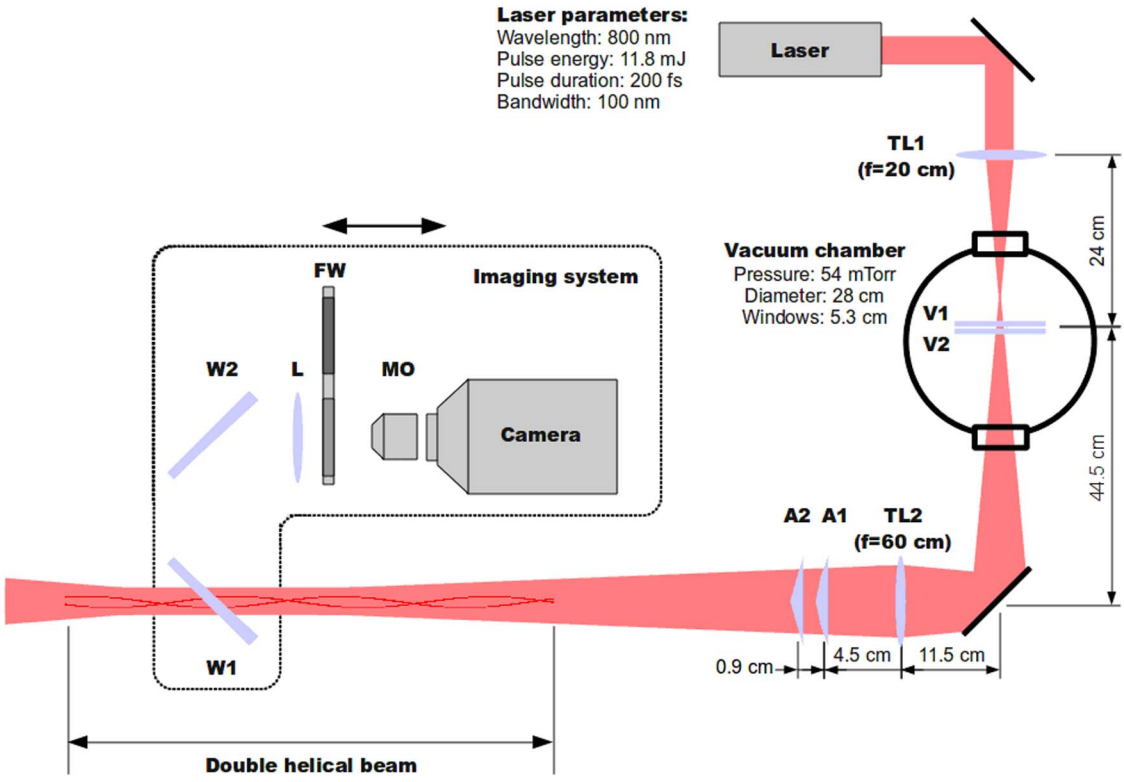

Fig. 4. (Color online) Experimental setup for the generation of helical beams.

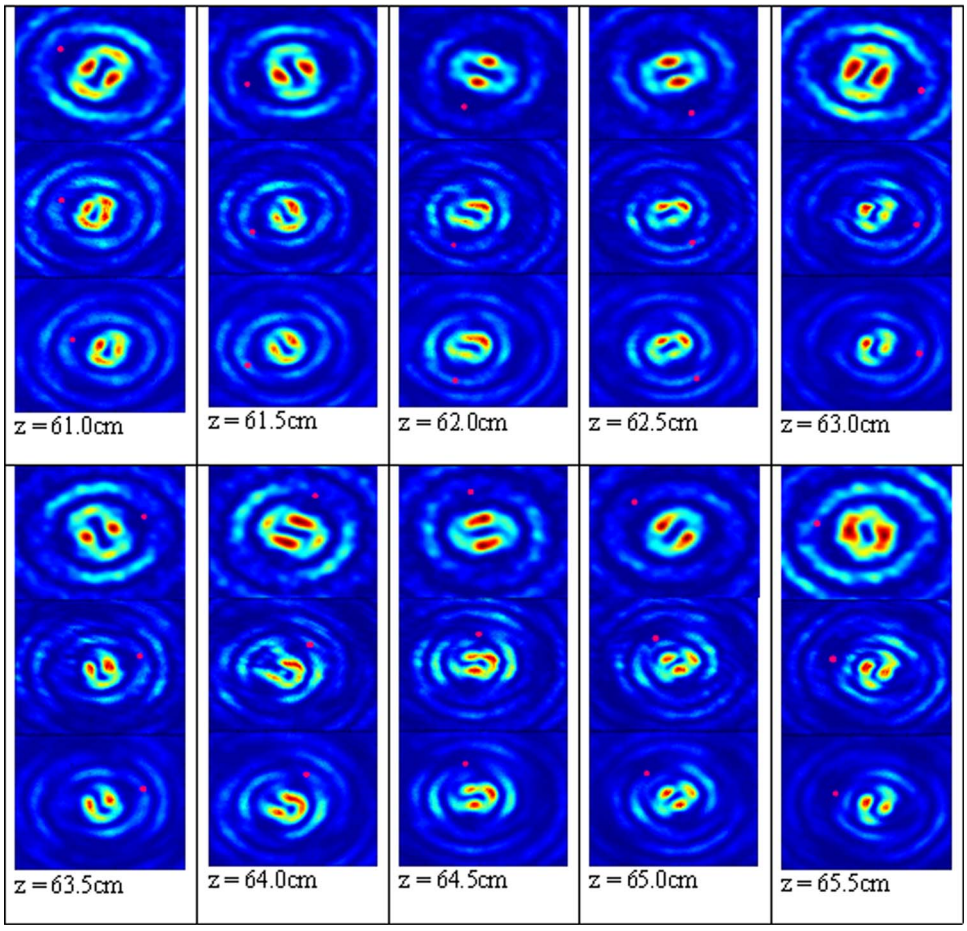

Fig. 5. (Color online) Transverse beam profiles of a helical beam at various points along the optical axis. The dot indicates rotation angle. Top, obtained from MATLAB simulation. Middle, obtained from experiments using continuous light. Bottom, obtained from experiments using pulses.

optical axis in 5 mm intervals. Measurements taken for the first 10 cm were analyzed in greater detail. Experimental results were compared against the numerical model.

Figure 5 shows the comparison between simulation and experimental results (continuous and pulsed) along one full rotation of the double helical beam. At each point along the optical axis, a double helical beam irradiance profile is observed. Sideband flares resulting from irradiance peaks present in the second ring associated with $J_1^2(r)$ are also present in many of the observed irradiance profiles. The helical beams are 125 μm in diameter, containing two 50 μm diameter irradiance peaks separated by a 25 μm null, falling within the 54 μm maximum size predicted by Eq. (23) for our experimental setup.

The experimental profiles have three key features in common with the simulation. Each experimental profile contains two identifiable irradiance peaks, although almost equally intense sidebands are present in some profiles. A clear null is present in the center of each beam. Also, the experimental profiles rotate in agreement with the images generated from simulation.

The rotation angle for both the simulation and experiment were obtained from the transverse irradiance profiles and are plotted in Fig. 6 as a function of propagation distance. Agreement between experiment and simulation can be observed directly from the plot. The plot indicates that the helical beam makes a complete rotation approximately every 4 cm. A similar conclusion can be drawn upon careful analysis of Fig. 5. This is consistent with Eq. (22), which predicts that, at a distance of 65 cm from the optical setup, the helical beam will make one complete rotation every 4.1 cm. However, variations in the rate of rotation as a consequence of the 2.1 m system focal length are not observed.

The experiment was repeated using ultrafast pulses. Helical beams were again observed between 60 and 80 cm from the second axicon. The transverse profiles of the pulsed helical beams obtained in our experiments are nearly identical to those obtained for the continuous case, as can be seen in Fig. 5, and exhibit the same rotation angle and rate, as can be seen in Fig. 6. The beam profiles obtained for the pulsed case exhibit a clearer pair of irradiance peaks and fewer irregularities than the continuous case. In effect, an improvement in irradiance profile of the structure is obtained by using pulsed beams in place of a continuous beam. This may be the a consequence of the Ti:sapphire laser used for both experiments, which is optimized for pulsed operation.

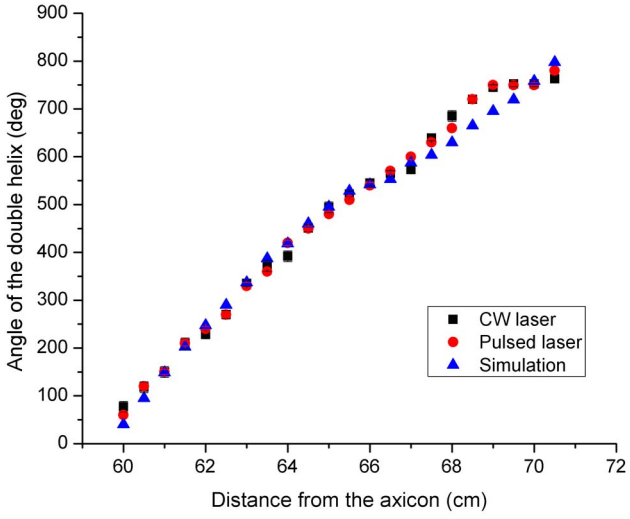

Fig. 6. (Color online) Rotation of the irradiance peaks of the double helical beam (see Fig. 5) as a function of propagation distance.

7. CONCLUSION

A serial arrangement for generating double helical beams through the interference of two first-order Bessel beams has been successfully demonstrated. Although this arrangement was devised through the application of linear diffraction theory to a continuous Gaussian beam, the configuration has also been demonstrated to operate with ultrafast pulses. A diffraction model was able to provide an adequate description of the double helical beam dimensions and rotation rate. The transverse beam profiles obtained through the simulation reproduced the basic structural features of the helical beam profiles obtained in the laboratory. These models can be extended to pulsed beams on a limited basis.

Experimentally obtained double helical beams produced rapid, consistent, and controlled rotations dictated by the optical setup in a manner consistent with analytical and numerical models. Double helical beam dimensions, rotation rate, and propagation distance can be readily altered by appropriate selection of optical elements.

ACKNOWLEDGMENTS

This work was funded by the U.S. Army Research Office (USARO) contract W911-NF-0910500, "Engineered laser filaments in air for defense stand-off sensing and interaction applications," and the State of Florida.

REFERENCES

1. J. Durnin and J. J. Miceli, Jr., "Diffraction-free beams," Phys. Rev. Lett. **58**, 1499–1501 (1987).
2. F. Gori, G. Guattari, and C. Padovani, "Bessel-Gauss beams," Opt. Commun. **64**, 491–494 (1987).
3. K. Ait-Ameur and F. Sanchez, "Gaussian beam conversion using an axicon," J. Mod. Opt. **46**, 1537–1548 (1999).
4. J. Pu, H. Zhang, and S. Nemoto, "Lens axicons illuminated by Gaussian beams for generation of uniform-axial intensity Bessel fields," Opt. Eng. **39**, 803–807 (2000).
5. R. Vasilyeu, A. Dudley, N. Khilo, and A. Forbes, "Generating superpositions of higher order Bessel beams," in *Frontiers in Optics*, OSA Technical Digest (CD) (Optical Society of America, 2009), paper FThB6.
6. J. Turunen, A. Vasara, and A. T. Friberg, "Holographic generation of diffraction-free beams," Appl. Opt. **27**, 3959–3962 (1988).
7. M. M. Mendez Otero, G. C. Martinez Jimenez, M. L. Arroyo Carrasco, M. D. Iturbe Catillo, and E. Marti Panameno, "Generation of Bessel-Gauss beams by means of computer-generated holograms for Bessel beams," in *Frontiers in Optics*, OSA Technical Digest (CD) (Optical Society of America, 2006), paper JWD129.
8. W.-X. Cong and N.-X. Chen, "Generation of nondiffracting beams by diffractive phase elements," J. Opt. Soc. Am. A **15**, 2362–2364 (1998).
9. S. Orlov, K. Regelskis, V. Smilgevicius, and A. Stabinis, "Propagation of Bessel beams carrying optical vortices, "Opt. Commun. **209**, 155–165 (2002).
10. M. W. Beijersbergen, R. P. C. Coerwinkel, M. Kristensen, and J. P. Woerdman, "Helical-wavefront laser beams produced with a spiral phase plate, Opt. Commun. **112**, 321–327 (1994).
11. J. Arlt and K. Dholakia, "Generation of high-order Bessel beams by use of an axicon," Opt. Commun. **177**, 297–301 (2000).

12. V. Jarutis, R. Paskauskas, and A. Stabinis, "Focusing of Laguerre–Gaussian beams by axicon," Opt. Commun. **184**, 105–112 (2000).
13. S. Chavez-Cerda, G. S. McDonald, and G. H. C. New, "Nondiffracting beams: travelling, standing, rotating and spiral waves," Opt. Commun. **123**, 225–233 (1996).
14. S. Chavez-Cerda, M. A. Meneses-Nava, and J. Miguel Hickmann, "Interference of traveling nondiffracting beams," Opt. Lett. **23**, 1871–1873 (1998).
15. T. Cizmar, V. Kollarova, X. Tsampoula, F. Gunn-Moore, Z. Bouchal, and K. Dholakia, "Generation and control of multiple Bessel beams for optical micromanipulation," Proc. SPIE **7038**, 70380Q (2008).
16. T. Cizmar, V. Kollarova, X. Tsampoula, F. Gunn-Moore, W. Sibbett, Z. Bouchal, and K. Dholakia, "Generation of multiple Bessel beams for a biophotonics workstation," Opt. Express **16**, 14024–14035 (2008).
17. C. Paterson and R. Smith, "Helicon waves: propagation-invariant waves in a rotating coordinate system," Opt. Commun. **124**, 131–140 (1996).
18. S. A. Baluyot and N. Hermosa II, "Intensity profiles and propagation of optical beams with bored helical phase," Opt. Express **17**, 16244–16254 (2009).
19. V. Jarutis, A. Matijosius, P. Di Trapani, and A. Piskarskas, "Spiraling zero-order Bessel beam," Opt. Lett. **34**, 2129–2131 (2009).
20. A. Matijosius, V. Jarutis, and A. Piskarskas, "Generation and control of the spiraling zero-order Bessel beam," Opt. Express **18**, 8767–8771 (2010).
21. S. A. Baluyot and N. Hermosa II, "Controllable rotation of optical beams with bored helical phases," Appl. Opt. **49**, 673–677 (2010).
22. L. Paterson, M. P. MacDonald, J. Arlt, W. Sibbett, P. E. Bryant, and K. Dholakia, "Controlled rotation of optically trapped microscopic particles," Science **292**, 912–914 (2001).
23. M. P. MacDonald, L. Paterson, K. Volke-Sepulveda, J. Arlt, W. Sibbett, and K. Dholakia, "Creation and manipulation of three-dimensional optically trapped structures," Science **296**, 1101–1103 (2002).
24. S.-H. Lee, Y. Roichman, and D. G. Grier, "Optical solenoid beams," Opt. Express **18**, 6988–6993 (2010).
25. K. W. Madison, F. Chevy, W. Wohlleben, and J. Dalibard, "Vortex formation in a stirred Bose-Einstein condensate," Phys. Rev. Lett. **84**, 806–809 (2000).
26. A. Greengard, Y. Y. Schechner, and R. Piestun, "Depth from diffracted rotation," Opt. Lett. **31**, 181–183 (2006).
27. S. R. P. Pavani, A. Greengard, and R. Piestun, "Three-dimensional localization with nanometer accuracy using a detector-limited double-helix point spread function system," Appl. Phys. Lett. **95**, 021103 (2009).
28. S. R. P. Pavani, M. A. Thompson, J. S. Biteen, S. J. Lord, N. Liu, R. J. Twieg, R. Piestun, and W. E. Moerner, "Three-dimensional, single-molecule fluorescence imaging beyond the diffraction limit by using a double-helix point spread function," Proc. Natl. Acad. Sci. USA **106**, 2995–2999 (2009).
29. C. Rotschild, M. Saraf, A. Barak, R. A. El-Ganainy, E. Lifshitz, D. N. Christodoulides, and M. Segev, "Complex nonlinear opto-fluidity," in *Conference on Lasers and Electro-Optics/Quantum Electronics and Laser Science Conference and Photonic Applications Systems Technologies*, OSA Technical Digest (CD) (2008), paper CPDA4.
30. T. Carmon, R. Uzdin, C. Pigier, Z. H. Musslimani, M. Segev, and A. Nepomnyashchy, "Rotating propeller solitons," Phys. Rev. Lett. **87**, 143901 (2001).
31. A. S. Desyatnikov and Y. S. Kivshar, "Rotating optical soliton clusters," Phys. Rev. Lett. **88**, 053901 (2002).
32. A. S. Desyatnikov, D. Buccoliero, M. R. Dennis, and Y. S. Kivshar, "Suppression of collapse for spiraling elliptic solitons," Phys. Rev. Lett. **104**, 053902 (2010).
33. A. Ya. Bekshaev, M. S. Soskin, and M. V. Vasnetsov, "Angular momentum of a rotating light beam," Opt. Commun. **249**, 367–378 (2005).
34. M. Pitchumani, H. Hockel, W. Mohammed, and E. G. Johnson, "Additive lithography for fabrication of diffractive optics," Appl. Opt. **41**, 6176–6181 (2002).